Momentum dependence of the single-particle self-energy and fluctuation spectrum of slightly underdoped $Bi_2Sr_2CaCu_2O_{8+\delta}$ from high-resolution laser angle-resolved photoemission

Jin Mo Bok, Jae Hyun Yun, and Han-Yong Choi
Department of Physics and Institute for Basic Science Research, SungKyunKwan University, Suwon 440-746, Korea

Wentao Zhang and X. J. Zhou
National Laboratory for Superconductivity, Beijing National Laboratory for Condensed Matter Physics, Institute of Physics, Chinese Academy of Sciences, Beijing 100190, China

Chandra M. Varma
Department of Physics and Astronomy, University of California, Riverside, California 92521, USA
(Received 30 November 2009; revised manuscript received 18 February 2010; published 17 May 2010)

We deduce the normal-state angle-resolved single-particle self-energy $\Sigma(\theta,\omega)$ and the Eliashberg function (i.e., the product of the fluctuation spectrum and its coupling to fermions) $\alpha^2F(\theta,\omega)$ for the high-temperature superconductor $Bi_2Sr_2CaCu_2O_{8+\delta}$ from the ultrahigh-resolution laser angle-resolved photoemission spectroscopy (ARPES). The self-energy $\Sigma(\theta,\omega)$ at energy ω along several cuts normal to the Fermi surface at the tilt angles θ with respect to the nodal direction in a slightly underdoped $Bi_2Sr_2CaCu_2O_{8+\delta}$ were extracted by fitting the ARPES momentum distribution curves. Then, using the extracted self-energy as the experimental input, the $\alpha^2F(\theta,\omega)$ is deduced by inverting the Eliashberg equation employing the adaptive maximum entropy method. Our principal result is that the Eliashberg functions $\alpha^2F(\theta,\omega)$ collapse for all θ onto a single function of ω up to the upper cut-off energy despite the θ dependence of the self-energy. The in-plane momentum anisotropy is therefore predominantly due to the anisotropic band-dispersion effects. The obtained Eliashberg function has a small peak at $\omega \approx 0.05$ eV and flattens out above 0.1 eV up to the angle-dependent cutoff. It takes the intrinsic cutoff of about 0.4 eV or the energy of the bottom of the band with respect to the Fermi energy in the direction θ, whichever is lower. The angle independence of the $\alpha^2F(\theta,\omega)$ is consistent only with the fluctuation spectra which have the short correlation length on the scale of the lattice constant. This implies among others that the antiferromagnetic fluctuations may not be the underlying physics of the deduced fluctuation spectrum.

DOI: 10.1103/PhysRevB.81.174516 PACS number(s): 74.25.Jb, 74.72.−h, 74.20.Mn

I. INTRODUCTION

It is generally agreed that understanding the normal-state properties is prerequisite to the high-temperature superconductivity because the pairing instability is a normal-state Fermi-surface instability. A number of studies have been conducted to elucidate the normal-state charge, spin dynamics, and momentum anisotropy of the high-temperature superconductors.[1–4] The angle-resolved photoemission spectroscopy (ARPES), owing to its unique momentum and energy resolution, has been quite powerful in uncovering the in-plane momentum anisotropy of the quasiparticle (qp) dynamics of the cuprates.[5] Early ARPES measurements[6] on optimally doped $Bi_2Sr_2CaCu_2O_{8+\delta}$ (Bi2212) and subsequent measurements[7–10] along the nodal cut of $(0,0)-(\pi,\pi)$ direction showed the marginal Fermi-liquid[11] behavior of $-\mathrm{Im}\,\Sigma(\omega) \propto \omega$ and found a kink around 0.06 eV in the qp dispersion. Kaminski *et al.*[12] extended these measurements to offnodal cuts to investigate the in-plane anisotropy of the qp scattering rate $-\mathrm{Im}\,\Sigma(\theta,\omega)$ around the Fermi surface. They reported that the functional form of the scattering rate for underdoped and optimally doped sample can be written as $a+b\omega$, where the elastic term $a(\theta)$ is anisotropic in correlation with the pseudogap, and the inelastic term, b, is isotropic around the Fermi surface; the scattering rates become isotropic for the heavily overdoped (OD) samples. On the other hand, Chang *et al.*[13] reported that both the elastic and inelastic terms are anisotropic, exhibiting a minimum along the nodal direction.

The in-plane anisotropy may also be probed by the angle-dependent magnetoresistance (ADMR) (Ref. 14) or the Raman-scattering experiments.[15] For instance, the polar ADMR measurements in OD $Tl_2Ba_2CuO_{6+\delta}$ (Tl2201) were analyzed in terms of the transport scattering rate Γ_{tr} which consists of the isotropic and anisotropic terms as

$$\Gamma_{tr}(\theta,T) = \Gamma_0(\theta) + \Gamma_1 \sin^2(2\theta)T + \Gamma_2 T^2, \tag{1}$$

where $\Gamma_0(\theta)$ is proportional to $1/v_F(\theta)$, i.e., the in-plane density of states.[16] The anisotropic T linear term, interestingly, has the same anisotropic form as the ω linear contribution to the Im Σ that Chang *et al.* reported, as mentioned above.

Besides its own significance, the momentum anisotropy of the single-particle self-energy is also necessary to understand the enormous amount of spectroscopic and transport properties of the cuprates. Moreover this self-energy is determined by coupling to the fluctuation spectra which is the essential physical quantity to understand in the cuprates. This may be done using the inversion of the Eliashberg equations provided the reliability of the approximations in the latter is checked consistently. Recently Schachinger and Carbotte[17] performed this inversion using the maximum entropy method (MEM) (Ref. 18) from the nodal cut ARPES data on Bi2212 of Zhang *et al.*[19] The obtained fluctuation spectra showed a

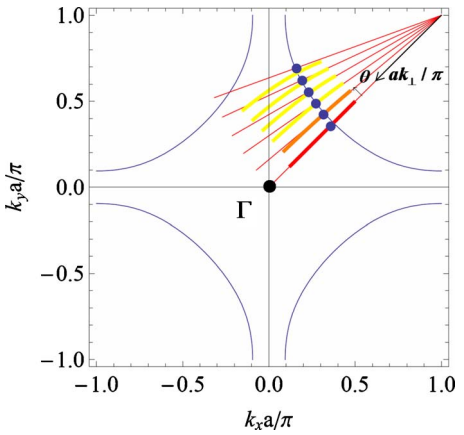

FIG. 1. (Color online) The Fermi surface of Bi2212 in the first Brillouin zone. The blue solid curves centered around the Γ point is the FS from Eq. (4) and the solid dots are the experimentally determined FS at $\theta=0°,5°,10°,15°,20°,25°$. $k_\perp$ is the distance from the (π,π) point. The thick bars along each cut indicate the ranges of experimentally measured ARPES MDC data. Parts of them which do not deviate much from the lines were actually used in the TB fitting as indicated in Fig. 4.

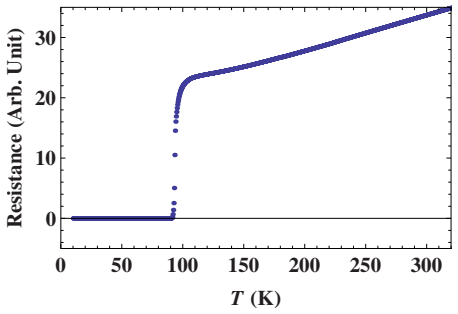

FIG. 2. (Color online) The temperature dependence of the resistivity of a slightly underdoped Bi2212 of $T_c=89$ K. T^* is estimated from the deviation from the linearity to be $T^*\approx 160$ K.

weak peak around 0.06 eV and a cutoff near 0.4 eV, which is similar to that obtained from the frequency-dependent conductivity on Bi2212.[20] This may be anticipated because the conductivity, being proportional to the Fermi velocity squared, is strongly weighted by contributions from near the nodal region. The analysis of the frequency-dependent conductivity in terms of the self-energy and Eliashberg function has been applied in many cases.[21–24]

However, the information obtained from the nodal direction alone is insufficient to characterize the self-energy and the momentum dependence of the fluctuation spectra. In the present work we analyze the momentum anisotropy and frequency dependence of the qp self-energy $\Sigma(\theta,\omega)$ in a slightly underdoped Bi2212 sample of $T_c=89$ K along the cuts of the tilt angles $\theta=0°,5°,10°,15°,20°,25°$ with respect to the nodal direction from (π,π) point in the Brillouin zone as shown in Fig. 1. The angle-resolved photoemission measurements have been carried out on a vacuum ultraviolet laser-based ARPES system.[25] In the experimental setup, there are two angles, θ and ϕ, to be controlled. They are then converted to the actual tilt angle $\tilde{\theta}$ and the amplitude $k_\perp$ of the inplane wave vector **k**. The $k_\perp$ in this paper is referred to the distance from the (π,π) point. The thick bars along the cuts of the Fig. 1 indicate the range of $k_\perp$ of the collected ARPES data as the angle ϕ is varied by approximately 30°. The actual tilt angle $\tilde{\theta}$ deviates slightly from the control tilde angle θ as the ϕ is varied. The change in θ is small and is disregarded in the analysis to be presented here. See the more technical discussion below Eq. (5) in sec. II.

The photon energy of the laser is 6.994 eV with a bandwidth of 0.26 meV. The energy resolution of the electron energy analyzer (Scienta R4000) is set at 1 meV, giving rise to an overall energy resolution of 1.03 meV which is significantly improved from regular 10–15 meV from regular synchrotron-radiation systems. The angular resolution is ~0.3°, corresponding to a momentum resolution ~0.004 $Å^{-1}$ at the photon energy of 6.994 eV, more than twice improved from 0.009 $Å^{-1}$ at a regular photon energy of 21.2 eV for the same angular resolution. The slightly underdoped Bi2212 single crystals with a superconducting transition temperature $T_c=89$ K were cleaved *in situ* in vacuum with a base pressure better than 5×10^{-11} Torr. The measurements were carried out at $T=107$ K which is below the pseudogap temperature T^*. The pseudogap temperature of the sample may be determined from the temperature dependence of the resistivity shown in Fig. 2. From the deviation from the T linearity of the resistivity, it is approximately $T^*\approx 160$ K in agreement with the independent estimate from different group.[26]

By the Lorentzian fitting of the ARPES momentum distribution curve (MDC) shown in Fig. 4, we extract the self-energy $\Sigma(\theta,\omega)$ (shown in Fig. 5 below) using a realistic tight-binding band dispersion [Eq. (4) below]. We confirm that the normal-state self-energy exhibits an in-plane momentum anisotropy in both the elastic and inelastic parts. Details will be presented in Sec. II. From the obtained self-energies, we extract the function α^2F by inverting the Eliashberg equation. We employ the adaptive maximum-entropy method. Its formulation is given in Sec. III. We show that in spite of the anisotropy in $\Sigma(\theta,\omega)$ the $\alpha^2F(\theta,\omega)$ obtained from data from the cuts at different θ's collapse onto a single curve (Fig. 7) at low energies with a cutoff at about 0.4 eV around the nodal direction changing smoothly to approximately 0.2 eV at 25°. The variation in the cutoff is simply accounted for by the variation in the position of the bottom of the band with respect to the Fermi energy with θ with the intrinsic cutoff of the spectrum of about 0.4 eV. Some of these results were anticipated by an approximate calculation[27] using an assumed spectra by analysis of ARPES in $La_{2-x}Sr_xCuO_4$ rather than the more reliable inversion method used here. These results put strong constraints on the momentum dependence of the fluctuation spectra, which we will discuss later. An implication of our results is that the anisotropy of the transport and spectroscopic properties originate simply from the anisotropy of the Fermi surface. The detailed results are presented in Sec. IV. In Sec. V, we will conclude with a discussion of the results, summary, and remarks motivating further work.

II. DEDUCING THE SELF-ENERGY

The ARPES intensity, within the sudden approximation, is given by

$$I(\mathbf{k},\omega) = |M(\mathbf{k},\nu)|^2 f(\omega)[A(\mathbf{k},\omega) + B(\mathbf{k},\omega)], \quad (2)$$

where $M(\mathbf{k},\nu)$ is the matrix element, ν the energy of incident photon, $f(\omega)$ the Fermi distribution function, A the qp spectral function, and B is the background. We write the in-plane momentum $\mathbf{k}$ with the $k_\perp$ perpendicular to the Fermi surface (FS) and the angle θ measured from the nodal cut as indicated in Fig. 1. Since Σ has a much weaker dependence on $k_\perp$ than ω (which is verified in the experiments through the Lorentzian distribution of the spectra as a function of $[k_\perp - k_F(\theta)]$, the spectral function may be rewritten as

$$A(\theta,k_\perp,\omega) = -\frac{1}{\pi}\frac{\Sigma_2(\theta,\omega)}{[\omega - \xi(\mathbf{k}) - \Sigma_1(\theta,\omega)]^2 + [\Sigma_2(\theta,\omega)]^2}. \quad (3)$$

Here, $\xi(\mathbf{k})$ is the bare dispersion, and Σ_1 and Σ_2 are, respectively, the real and imaginary parts of the self-energy. Along a cut with a fixed tilt angle θ, then, the dependence on $k_\perp$ is solely through the bare dispersion energy $\xi(\mathbf{k})$. A has a Lorentzian form with respect to $\xi(\mathbf{k})$. The self-energy can be directly extracted from the ARPES intensity by a Lorentzian fit if $\xi(\mathbf{k})$ is known.

We first determined the tight-binding (TB) dispersion of $\xi(\mathbf{k})$ by matching the experimental Fermi surface with the four parameter dispersion.

$$\xi(k_x,k_y) = -2t(\cos k_x a + \cos k_y a) + 4t' \cos k_x a \cos k_y a - 2t''(\cos 2k_x a + \cos 2k_y a) - \mu, \quad (4)$$

where $a=3.82$ Å is the lattice constant and μ is the chemical potential. We took $t=0.395$, $t'=0.084$, $t''=0.042$, and $\mu=-0.43$ eV, which are consistent with Kordyuk *et al.*[28] Note that we neglected the bilayer splitting present in the Bi2212 compounds. At the photon energy used ($h\nu=6.994$ eV) in the laser ARPES, only the antibonding bands are observed and the bonding band is completely suppressed. The experimentally determined FS in comparison with that from Eq. (4) is shown in Fig. 1. The six cuts with the tilt angles θ with respect to the (π,π) are also shown with the solid lines. To study the importance of the bare dispersion ξ we also used the linear dispersion (LD) for comparison.

$$\xi(\mathbf{k}) = v_F(\theta)[k_\perp - k_F(\theta)], \quad (5)$$

where v_F and k_F were calculated from the tight-binding dispersion of Eq. (4).

In order are some technical points about the cuts perpendicular to the Fermi surface. In the ARPES experiment setup, two angles are the control parameters: one is the tilt angle θ which closely corresponds to the actual tilt angle $\tilde{\theta}$ and the other is ϕ which determine the $k_\perp$ such that

$$k_0 = \frac{\sqrt{2mE_{kin}}}{\hbar}, \quad k_x = k_0 \sin\phi, \quad k_y = k_0 \cos\phi \sin\theta, \quad (6)$$

where E_{kin} is the kinetic energy of the photoelectons given by

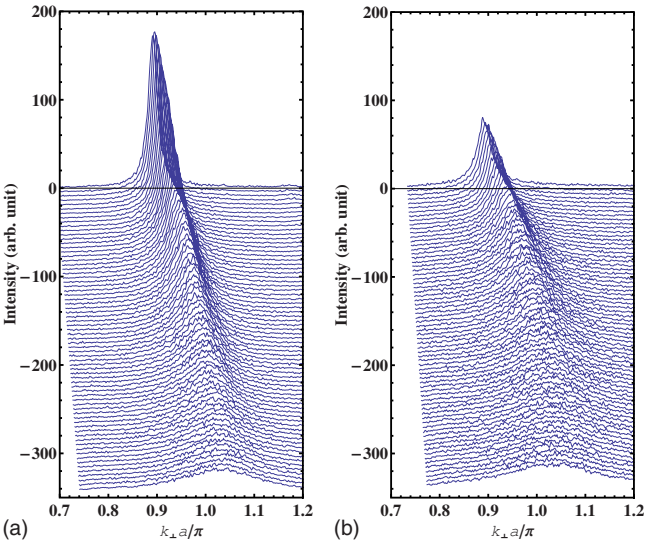

FIG. 3. (Color online) The representative MDC as a function of the momentum perpendicular to the FS, $k_\perp a/\pi$, and their dispersion as the binding energy is varied. Each curve is shifted down for clarity. The left plot is for the tilt angle 5° and the right for 20°. From the top to bottom are the MDC at the energy $\omega=0.0005$ eV with the step of 0.005 eV up to 0.3455 eV. The qp coherence peak becomes suppressed as the energy is increased away from the Fermi level or the tilt angle increased from the nodal cut.

$$E_{kin} = h\nu - W - |\omega|, \quad (7)$$

where $W=4.3$ eV is the work function. The k_x and k_y are the components of the wave vector of the photoelectron with respect to the diagonal cuts. The $k_\perp$, which is the distance from the (π,π) point can be simply calculated by the trigonometry. The ϕ is varied by approximately 30° and the corresponding $k_\perp$ which go through the Fermi surface is shown by the thick bars in Fig. 1. A consequence of this experimental setup is that the actual tilt angle $\tilde{\theta}$ is not constant as given by the θ. $\tilde{\theta}=\theta$ for $\theta=0$, but $\tilde{\theta}$ begins to deviate from θ as ϕ is varied when $\theta\neq 0$. The actual cuts therefore are not straight lines but slightly curved for large $k_\perp$ as shown in Fig. 1 but for $k_\perp$ near the Fermi surface the cuts point to the (π,π) direction. We disregard the difference between the $\tilde{\theta}$ and θ, and use θ to denote the tilt angle in this paper.

Typical ARPES intensity as a function of $k_\perp$ for fixed tilt angles and binding energy, referred to as the momentum-distribution curve, and the dispersion as a function of the binding energy ω are shown in Fig. 3. Each curve is shifted down for clarity as the binding energy is varied. The left and right plots are, respectively, for the tilt angle 5° and 20°. From the top to bottom are the MDC at the energy $\omega=0.0005$ eV with the step of 0.005 eV up to 0.3455 eV. Note that the qp coherence peak becomes suppressed as the energy is increased away from the Fermi level or the tilt angle increased from the nodal cut. These MDC were fitted by equating the ARPES intensity with the spectral function given by Eq. (3) as

$$I(\theta,k_\perp,\omega) = CA(\theta,k_\perp,\omega) + B(\theta,\omega) \quad (8)$$

to extract the self-energy as a function of the energy for a given cut.

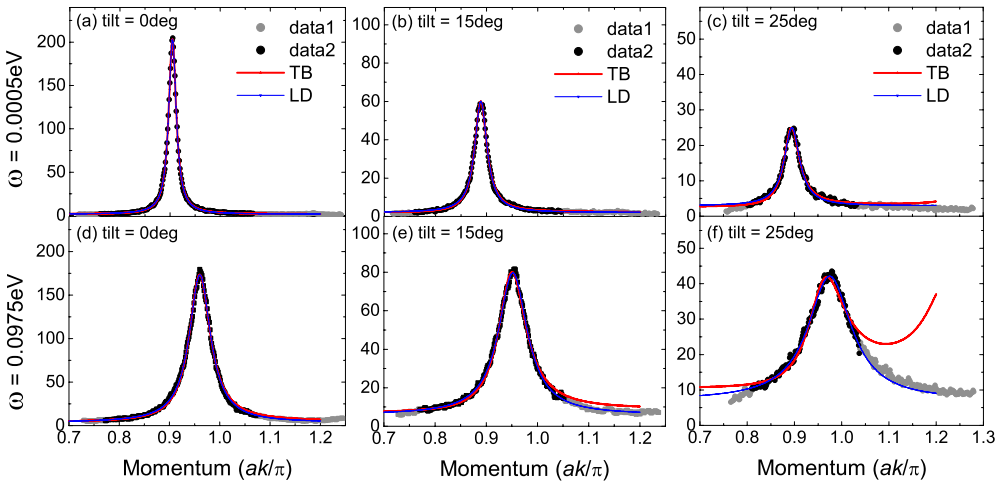

FIG. 4. (Color online) The representative momentum-distribution curves as a function of the momentum perpendicular to the FS, $k_\perp a/\pi$, at the tilt angles θ=0, 15°, and 25°, and the binding energy ω=0.0005 and 0.0975 eV. The shaded circles are the experimental ARPES intensities and the solids ones are those used in the fitting. The red and blue lines are the fitting with the TB and LD bands, respectively. Note that the MDC is not Lorentzian when plotted as a function of $k_\perp$ with the TB dispersion as can clearly be seen from (f).

In Fig. 4, we show the MDC fits for the nodal (θ=0°), θ=15°, and θ=25° cuts and for the binding energy ω =0.0005 (the Fermi level) and ω=0.0975 eV as representative cases. The shaded dots are the experimental ARPES intensities and the solid dots are those used in the fitting. The thick red and thin blue lines are the spectral function of Eq. (3) with the TB and LD bands, respectively. From the peak position and the width of the peak together with the bare dispersion $\xi(\mathbf{k})$, we can determine the real and imaginary parts of the self-energy.

The self-energies, $-\Sigma_1(\theta,\omega)$ and $\Sigma_2(\theta,\omega)$ for $\omega>0$, determined this way at T=107 K are shown in Fig. 5. The plot (a) was obtained using the TB and the plot (b) using the LD band. The real parts of the self-energy, $\Sigma_1(\omega)$, cross the zero at progressively smaller energies as the tilt angle is increased. This feature is more pronounced in the TB dispersion analysis as can be seen by comparing the plots (a) and (b), and is better described by the TB because the band bottom cannot be captured by the LD. The imaginary parts of the self-energy decrease monotonically as ω is increased up to ω=0.45 eV. The elastic part, $\Sigma_2(\theta,\omega=0)$, clearly changes as θ is changed. The elastic qp scattering rate is momentum anisotropic in accord with previous works.[12–14] The functional dependence of the qp scattering rates on the θ and ω for small ω may be analyzed in analogy with the Eq. (1). We confirm that both elastic and inelastic qp scattering rates exhibit an anisotropy as a function of angle θ around the Fermi surface.

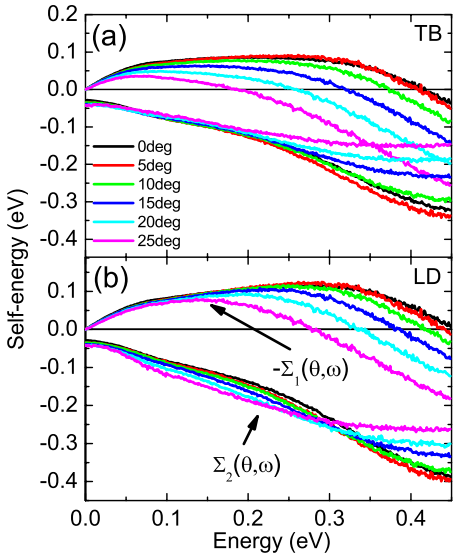

FIG. 5. (Color online) The real and imaginary part self-energies at T=107 K for the tilt angles θ=0, 5°, 10°, 15°, 20°, and 25°. $-\Sigma_1$ and Σ_2 as a function of the positive energy ω are shown. Plot (a) shows the extracted self-energy using the TB dispersion and (b) shows, for comparison, one using the linear dispersion.

The extracted self-energies were used as an input to deduce the fluctuation spectral functions by inverting the Eliashberg equation. It will be presented in the following section. Before the detailed analysis, we note that the relation

$$-\frac{\partial\Sigma_2(\theta,\omega)}{\partial\omega}=\pi\alpha^2F(\theta,\omega) \tag{9}$$

holds for $\omega\gg T$, as may be deduced from Eq. (12) below. The extracted $\Sigma_2(\theta,\omega)$ from the TB collapse onto a single curve up to $\omega\lesssim 0.2$ eV as can be seen from Fig. 5. This, together with Eq. (9), suggests that the Eliashberg function $\alpha^2F(\theta,\omega)$ would yield a single-curve independent of the tilt angle θ for $T\ll\omega\lesssim 0.2$ eV. The detailed analysis presented in the following sections will establish that the Eliashberg function $\alpha^2F(\theta,\omega)$ at different angle θ collapse onto a single function of ω with the intrinsic cutoff of about 0.4 eV or the energy of the band bottom in direction θ with respect to the Fermi energy, whichever is smaller. This is our key result which we will turn to.

III. DEDUCING THE FLUCTUATION SPECTRA: FORMULATION

Neglecting vertex corrections (justification for this will be given in the concluding section), the self-energy $\Sigma(\mathbf{k},\omega)$ may be written as

$$\Sigma(\mathbf{k},\omega) = \int_{-\infty}^{\infty} d\epsilon \int_{-\infty}^{\infty} d\epsilon' \frac{f(\epsilon)+n(-\epsilon')}{\epsilon+\epsilon'-\omega-\imath\delta} \times \sum_{\mathbf{k}'} A(\mathbf{k}',\epsilon)\alpha^2(\mathbf{k},\mathbf{k}')F(\mathbf{k}',\mathbf{k},\epsilon'), \quad (10)$$

where f and n represent the Fermi and Bose distribution function, respectively. $\alpha(\mathbf{k},\mathbf{k}')$ is the matrix element for scattering fermions with the fluctuations of spectral weight $F(\mathbf{k}',\mathbf{k},\epsilon)$. After the integral over $k'_{\perp}$, the real and imaginary parts are given by

$$\Sigma_1(\theta,\omega) = \int_{-\infty}^{\infty} d\epsilon' \int_{-\infty}^{\infty} d\epsilon \frac{f(\epsilon)+n(-\epsilon')}{\epsilon+\epsilon'-\omega}\alpha^2F(\theta,\epsilon'), \quad (11)$$

$$\Sigma_2(\theta,\omega) = \pi\int_{-\infty}^{\infty} d\epsilon'[f(\omega-\epsilon')+n(-\epsilon')]\alpha^2F(\theta,\epsilon'), \quad (12)$$

where the Eliashberg function or the bosonic coupling spectrum, $\alpha^2F(\theta,\epsilon')$ is given by

$$\alpha^2F(\theta,\epsilon') \equiv \left\langle \frac{\alpha^2(\theta,\theta')}{v_F(\theta')}F(\theta,\theta',\epsilon') \right\rangle_{\theta'}. \quad (13)$$

The $v_F(\theta')$ is the angle-dependent Fermi velocity and the bracket implies the angular average. We can extract the "averaged" spectrum $\alpha^2F(\theta,\epsilon')$ by inverting either Eq. (11) and (12). Thus information only about the angle dependence of the average over the product of the squared matrix element and spectra as constrained by energy-momentum conservation are obtained. Both equations must give the same results for $\alpha^2F(\theta,\omega)$ provided the real and imaginary parts of the self-energy satisfy the Kramers-Kronig (KK) relation. In the present case, however, the extracted spectra do depend on whether it is extracted from the real or imaginary part. It implies that the extracted real and imaginary parts of the self-energy do not satisfy the KK to the required accuracy. It turned out that the α^2F from the real-part self-energy is more reliable as shown below, probably because the peak position of MDC is better determined than the width. This point was also noted by Shi *et al.*[18]

A few techniques have been devised to invert the Eliashberg Eq. (11) and (12). We employ the MEM.[18,29] It is a useful technique to overcome the numerical instability in the direct inversion, by incorporating the physical constraints into the fitting process. The MEM minimizes the functional

$$L = \frac{\chi^2}{2} - \alpha S. \quad (14)$$

The χ^2 is the error and S is the generalized Shannon-Jaynes entropy defined below. The multiplier α is a determinative parameter that controls how close the fitting should follow the data while not violating the physical constraints. When α is small, the fitting will follow the data as closely as possible at the expense of a noisy and/or negative Eliashberg function, and when α is large, the extracted Eliashberg function will not deviate much from the constraint function $m(\epsilon')$. For a given tilt angle θ, we take

$$\chi^2 = \sum_{i=1}^{N_D} \frac{[D_i - \Sigma_1(\omega_i)]^2}{\sigma_i^2}, \quad (15)$$

$$S = \int_0^{\infty} d\epsilon' \left[\alpha^2F(\epsilon') - m(\epsilon') - \alpha^2F(\epsilon')\ln\frac{\alpha^2F(\epsilon')}{m(\epsilon')} \right], \quad (16)$$

where N_D is the total number of data points, D_i is the experimental data for the real part of the self-energy at the energy ω_i, $\Sigma_1(\theta,\omega_i)$ is defined by Eq. (11), and σ_i is the error bars of the data. The entropy term imposes physical constraints to the fitting and is maximized when $\alpha^2F(\epsilon')=m(\epsilon')$, where $m(\epsilon')$ is the constraint function. To minimize Eq. (14) for a given $m(\epsilon')$, the Eliashberg function $\alpha^2F(\omega_j)$ is optimized in each iterative step by updating it as

$$\delta F_j = -\sum_k A_{jk}^{-1}\frac{\delta L}{\delta F_k}, \quad A_{jk} = \frac{\delta^2 L}{\delta F_j \delta F_k}, \quad (17)$$

where $F_j=\alpha^2F(\omega_j)$. The matrix inversion of A_{jk}^{-1} was performed using the singular value decomposition technique. Details of the algorithms can be found in Ref. 29.

In usual MEM approaches, the constraint function is chosen based on our best *a priori* knowledge for the specific system and remains unaltered. The obtained results for $\alpha^2F(\epsilon')$ do depend on how the m was chosen. In order to decrease the dependence on the constraint function and also to better represent the physical system, we employ the adaptive MEM which was implemented as follows: for a chosen constraint function $m(\epsilon')$, the iterative minimization is performed as described above. After the convergence, the $m(\epsilon')$ is updated to a linear combination of $m(\epsilon')$ and $\alpha^2F(\epsilon')$ to reflect the nature of the solution. For this new constraint function, the minimization is performed again via iterations. This second optimization is repeated until the convergence is reached. The double iterative adaptive MEM decreases the dependence on the choice of the constraint function and improves the overall fitting quality. The quality of the adaptive MEM can be seen by comparing the real-part self-energy from the ARPES data and the self-energy expression of Eq. (11) as shown in Fig. 6.

IV. FLUCTUATIONS SPECTRA

As noted previously, the real part of the self-energy is determined more accurately from the ARPES intensity and as the tilt angle is varied the tight-binding dispersion is more reliable. We therefore present in Fig. 7 the Eliashberg function $\alpha^2F(\theta,\omega)$ extracted from the real-part self-energy determined using the TB dispersion shown in Fig. 5. Note that structures in $\Sigma(\theta,\omega)$ are reflected in the coupled fluctuation

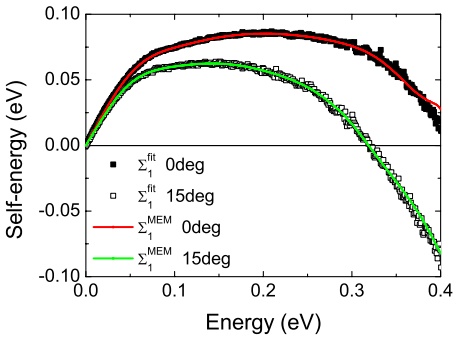

FIG. 6. (Color online) Comparison between the real part of the self-energy and the MEM fitting of Eq. (11) for the tilt angles $\theta=0°$ and 15°. The squares are the extracted real part self-energy of Fig. 5(a) and the solid lines are the MEM fitting.

spectra $\alpha^2F(\theta,\omega)$. The Eliashberg functions increase approximately linearly from zero as ω is increased and have a peak at $\omega\approx0.05$ eV, flattens above 0.1 eV, and vanishes above a cut-off energy ω_c which does depend on θ. The noisy feature above 0.35 eV is the numerical artifacts of the singular value decomposition and MEM. The cut-off energy is approximately 0.37 eV along the nodal cut. These are in good agreement with Schachinger and Carbotte[17] who analyzed the nodal cut Bi2212 laser ARPES data for the same sample.[19]

Now we discuss the new results of the analysis of the off-nodal cuts. The Eliashberg functions obtained are presented in Fig. 7 for the tilt angles $\theta=0°,5°,10°,15°,20°,25°$. As the tilt angle is increased, the peak energy remains unaltered but the cut-off energy decreases monotonically. At $\theta=25°$, $\omega_c\approx0.25$ eV. With Laser ARPES the data at large angles is not obtainable due to kinetic constraints; moreover the problems presented in the analysis due to interference of data due to the contributions from the next zone, as is obvious from Fig. 1, become more serious. An important point may be noted from comparison of Figs. 7 and 8 where the position of the band bottom with respect to the Fermi energy is given. The latter is about 1 eV in the nodal direction and about 0.25 eV at $\theta\approx25°$. As was shown in a simple calculation[27] and as is natural, the band bottom serves as an effective cutoff in the fluctuation spectrum when it is lower than the intrinsic cutoff. So one important results is that the intrinsic cutoff of the spectrum is about 0.4 eV. An even more important result contained in Fig. 7 is that quite remarkably the fluctuation spectra for different tilt angles collapse onto a single curve below the angle-dependent *effective* cutoff. Note that the corresponding self-energies do change even at low energies as the angle is varied as can be seen from Fig. 5. From Eq. (11) it follows that a nearly isotropic $\alpha^2F(\theta,\omega)$ produces an angle-dependent self-energy purely from the effects of the dispersion of the bare band.

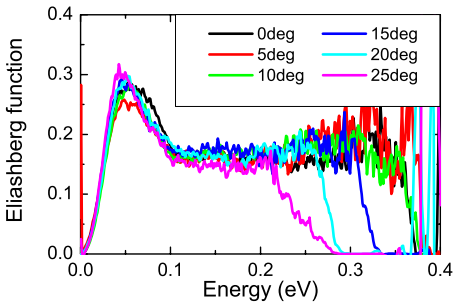

FIG. 7. (Color online) The Eliashberg function extracted from the real part of the self-energy at $T=107$ K. Notice the remarkable collapse of the Eliashberg functions below $\omega\approx0.2$ eV for different tilt angles.

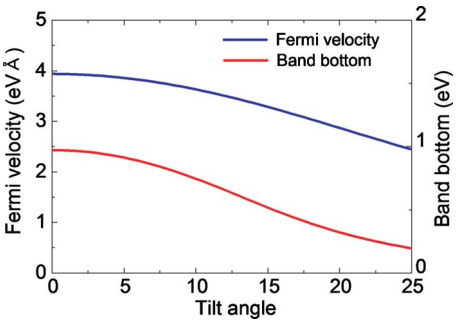

FIG. 8. (Color online) The angle dependence of the Fermi velocity and band bottom calculated from Eq. (4).

The Eliashberg functions may also be extracted from the imaginary parts of the self-energy using Eq. (12). The results are given in Fig. 9 for the tilt angles 0° and 15° for representative cases. As alluded before, they do not agree exactly with those from the real parts of the self-energy. Especially the features around the cutoff are exaggerated in the $\alpha^2F(\theta,\omega)$ from the imaginary part self-energies. The $\alpha^2F(\theta,\omega)$ do not collapse as neatly as those from the real parts. Also shown are the $-\frac{1}{\pi}\frac{\partial\Sigma_2(\omega)}{\partial\omega}$ for the same tilt angles. The $-\frac{1}{\pi}\frac{\partial\Sigma_2(\omega)}{\partial\omega}$ and $\alpha^2F(\omega)$ determined from $\Sigma_2(\omega)$ agree overall as expected.

V. DISCUSSION OF RESULTS, CONCLUSIONS, AND GUIDES TO FURTHER EXPERIMENTS

In this section, we discuss the implications of our findings which point to future experiments and analysis. They are the

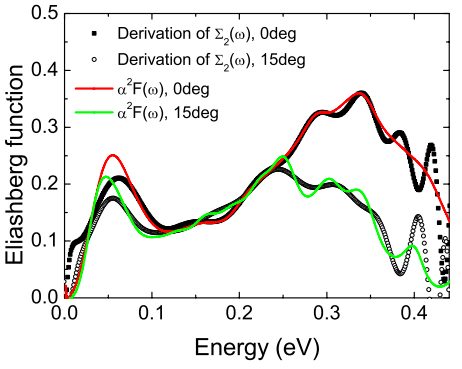

FIG. 9. (Color online) The Eliashberg function deduced from the imaginary parts of the self-energy. Results for $\theta=0°$ and 15° are given for representative cases. Also shown are $-\frac{1}{\pi}\frac{\partial\Sigma_2(\omega)}{\partial\omega}$. They agree overall as expected.

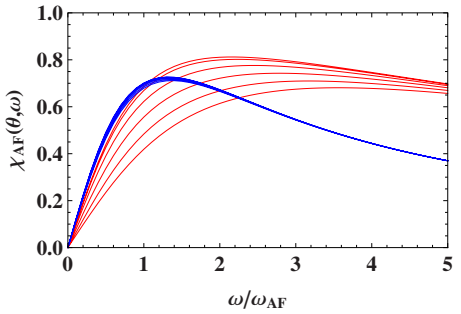

FIG. 10. (Color online) The model Eliashberg function calculated from the overdamped AF fluctuations of Eq. (18). The red and blue lines are for the AF correlation length $\xi/a=1$ and $1/\pi$, respectively. For each ξ, the angles are from above $\theta=0$, 5°, 10°, 15°, 20°, and 25°. As ξ is decreased the fluctuation spectra become momentum isotropic.

angle independence of the Eliashberg function $\alpha^2F(\theta,\omega)$, i.e., the angle averaged product of the matrix element and the spectral function of the fluctuations, as defined in Eq. (13), the possible physics of the low-energy bump around ≈ 0.05 eV, the vertex corrections to the Eliashberg equation, and various other assorted issues. The finding that the Eliashberg function is angle independent below the cutoff ω_c puts an important constraint on the microscopic understanding of the cuprates. For example, it can put a limit on the correlation length ξ for the commonly assumed form of the antiferromagnetic (AF) fluctuations. A phenomenological form of the overdamped AF fluctuations may be written as[2,30]

$$\chi_{AF}(\mathbf{k},\mathbf{k}',\omega)=\frac{\alpha\xi^2\omega/\omega_{AF}}{[(\mathbf{k}-\mathbf{k}'-\mathbf{Q})^2\xi^2+1]^2+(\omega/\omega_{AF})^2}. \quad (18)$$

$\chi_{AF}(\theta,\omega)$ can be obtained after the integral over θ' with both $\mathbf{k}$ and $\mathbf{k}'$ on the Fermi surface, that is,

$$\chi_{AF}(\theta,\omega)=\langle\chi_{AF}(\mathbf{k},\mathbf{k}',\omega)\rangle_{\theta'}, \quad (19)$$

where $\mathbf{k}$ and $\mathbf{k}'$ have the angle θ and θ' with respect to the nodal cut, respectively. A straightforward calculation reveals that a weak θ dependence of $\chi_{AF}(\theta,\omega)$ means that $\xi/a\ll 1$ for $\omega\lesssim\omega_{AF}$, where ω_{AF} is the characteristic AF energy scale. This is shown in Fig. 10 for $\xi/a=1/\pi$ with the blue and for $\xi/a=1$ with the red lines. For each ξ, the angles are $\theta=0°,5°,10°,15°,20°,25°$ from above. As expected, $\chi_{AF}(\theta,\omega)$ becomes angle independent as ξ is decreased. The collapse of $\alpha^2F(\theta,\omega)$ implies that if it is due to the AF fluctuations, the AF correlation length should be $\xi/a\lesssim 1/\pi$ for Bi2212 at $T=107$. This is an upper limit since we have not included the angle dependence of the matrix elements of coupling of AF fluctuation to fermions which enters Eq. (13). A correlation length less than a lattice constant is indicative either that there is negligible spectral weight in AF fluctuations or that they couple to single-particle excitations weakly enough to have no observable effect. This implies among others that the antiferromagnetic fluctuations may not be underlying physics of the deduced fluctuation spectrum. This also means that the scenario of "hot" and "cold" spots on the Fermi surface is inapplicable to the cuprates.

An angle-independent $\alpha^2F(\theta,\omega)$ is consistent with the quantum-critical spectra hypothesized in the marginal Fermi-liquid description of cuprates and recently derived microscopically[31,32] to be the spectra in the quantum-critical region of the phase diagram of the cuprates due to the quantum melting of the loop-current order observed[33–36] in the underdoped region of the cuprates. There is one aspect of the deduced $\alpha^2F(\theta,\omega)$ which is not given by the theory. This is the low-energy bump at the energy of $\omega\approx 0.05$ eV. The presence of this bump may be seen directly in the deduced Im $\Sigma(\theta,\omega)$ which is not linear as a function of ω for low $\omega\gg T$. The linearity may be expected on the basis of such theory and earlier ARPES experiments which, however, do not have the high resolution of the present experiments. If the bump occurs only in samples studied in the pseudogap region, there must exist collective modes special to this region of the phase diagram. This can be checked by equally high-resolution data in samples in the quantum-critical region or the overdoped region of the phase diagram.

We now discuss the validity of the neglect of vertex correction in the relation of the self-energy and the fluctuations. The exact relation between the vertex correction $\delta\Lambda(\mathbf{k},\mathbf{q},\omega,\nu)$ and the self-energy is that

$$\delta\Lambda(\mathbf{k},\mathbf{q},\omega,\nu)=\Sigma(\mathbf{k}+\mathbf{q},\omega+\nu)-\Sigma(\mathbf{k},\omega). \quad (20)$$

As discussed, the experiments give at energies up to about 0.2 eV, that the self-energy has a momentum dependence due only to the anisotropy of the Fermi velocity, which from Fig. 8 is only about 20%. This may be regarded as negligible. It therefore follows that the momentum dependence of the vertex correction is negligible. This means that all the essential conclusions about the momentum independence of the fluctuation spectra arrived at here remain valid. As regards the frequency dependence, there is indeed a vertex correction which in dimensionless form is of $O(\alpha^2\omega_c/W)$, where ω_c is the upper cutoff of the fluctuations and W is the electronic bandwidth of about 2 eV. For $\alpha^2\approx 1$, there are then vertex corrections of $O(1/5)$. This means that our *quantitative* conclusions have a validity no better than about 20%.

One final remark pertains to the information that the deduced spectra offers for the fluctuations spectra responsible for the superconductive instability. The normal-state single-particle self-energy has the full symmetry of the lattice. It then follows, as is visible from Eq. (10) that the "$\ell=2$" part of the fluctuation spectrum, which determines the symmetry of the superconductivity in cuprates is not visible through study of the normal state. It is unlikely that a completely different form of the spectra is responsible for the normal state and the superconducting state. A test of this conjecture and the deduction unambiguously of the spectra responsible for superconductivity requires a study of the variation in the single-particle self-energy as a function of energy on going from the normal to the superconducting state. This would be a generalization[37] of the McMillan-Rowell procedure[38] to d-wave superconductors requiring high-resolution ARPES. Such work is in progress.

To summarize, we have presented the self-energy analysis from the ultrahigh-resolution laser ARPES on the slightly-underdoped Bi2212 high-temperature superconductors. The

self-energy was determined along the nodal and off-nodal cuts in the normal state. Both the elastic and inelastic quasiparticle scattering rates exhibit in-plane momentum anisotropy. The deduced self-energies were then used as an experimental input to invert the Eliashberg equation to extract the product of the fluctuation spectra and the coupling to the single particles. The adaptive MEM was used. The high-resolution ARPES data together with the realistic tight-binding band dispersion enabled us to determine high-quality self-energy and the Eliashberg function. At the temperature $T=107$ K between the superconducting T_c and pseudogap temperature T^*, the Eliashberg functions for different tilt angles collapse onto a single curve up to the upper cutoff despite the angle-dependent self-energy. The cutoff has an intrinsic value of about 0.4 eV or the band-bottom energy with respect to the Fermi level if it is less than about 0.4 eV. The implications of our results have also been discussed.

ACKNOWLEDGMENTS

J.M.B., J.H.Y., and H.Y.C. acknowledge the support from Korea Research Foundation (KRF) under Grant No. KRF-C00241. X.J.Z. is grateful for the support by the NSFC, the MOST of China (973 Projects No. 2006CB601002 and 2006CB921302). X.J.Z. also thanks Sheng Bing and Hai-hu Wen for their help in resistivity measurement. C.M.V.'s work is partially supported under Grant No. DMR-0906530 of the U.S. National Science Foundation.

[1] A. Cho, Science **314**, 1072 (2006).
[2] A. V. Chubukov, D. Pines, and J. Schmalian, in *The Physics of Superconductors*, edited by K. H. Bennemann and J. B. Ketterson (Springer, Berlin, 2003), Vol. 2.
[3] D. N. Basov and T. Timusk, Rev. Mod. Phys. **77**, 721 (2005).
[4] N. E. Hussey, J. Phys. Condens. Matter **20**, 123201 (2008).
[5] A. Damascelli, Z. Hussain, and Z.-X. Shen, Rev. Mod. Phys. **75**, 473 (2003).
[6] T. Valla, A. V. Fedorov, P. D. Johnson, B. O. Wells, S. L. Hulbert, Q. Li, G. D. Gu, and N. Koshizuka, Science **285**, 2110 (1999).
[7] P. V. Bogdanov *et al.*, Phys. Rev. Lett. **85**, 2581 (2000).
[8] A. Kaminski *et al.*, Phys. Rev. Lett. **84**, 1788 (2000).
[9] A. Lanzara *et al.*, Nature (London) **412**, 510 (2001).
[10] X. J. Zhou *et al.*, Nature (London) **423**, 398 (2003).
[11] C. M. Varma, P. B. Littlewood, S. Schmitt-Rink, E. Abrahams, and A. E. Ruckenstein, Phys. Rev. Lett. **63**, 1996 (1989).
[12] A. Kaminski *et al.*, Phys. Rev. B **71**, 014517 (2005).
[13] J. Chang *et al.*, Phys. Rev. B **78**, 205103 (2008).
[14] M. Abdel-Jawad, J. G. Analytis, L. Balicas, A. Carrington, J. P. H. Charmant, M. M. J. French, and N. E. Hussey, Phys. Rev. Lett. **99**, 107002 (2007).
[15] T. P. Devereaux and R. Hackl, Rev. Mod. Phys. **79**, 175 (2007).
[16] C. M. Varma and E. Abrahams, Phys. Rev. Lett. **86**, 4652 (2001).
[17] E. Schachinger and J. P. Carbotte, Phys. Rev. B **77**, 094524 (2008).
[18] J. Shi *et al.*, Phys. Rev. Lett. **92**, 186401 (2004).
[19] W. Zhang *et al.*, Phys. Rev. Lett. **101**, 017002 (2008).
[20] J. Hwang, T. Timusk, E. Schachinger, and J. P. Carbotte, Phys. Rev. B **75**, 144508 (2007).
[21] T. Gimm and H. Choi, arXiv:cond-mat/0212361 (unpublished).
[22] H.-Y. Choi and T.-H. Gimm, Int. J. Mod. Phys. B **17**, 3534 (2003).
[23] S. V. Dordevic, L. W. Kohlman, N. Stojilovic, R. Hu, and C. Petrovic, Phys. Rev. B **80**, 115114 (2009).
[24] E. van Heumen, E. Muhlethaler, A. B. Kuzmenko, H. Eisaki, W. Meevasana, M. Greven, and D. van der Marel, Phys. Rev. B **79**, 184512 (2009).
[25] G. D. Liu *et al.*, Rev. Sci. Instrum. **79**, 023105 (2008).
[26] A. Kanigel *et al.*, Nat. Phys. **2**, 447 (2006).
[27] L. Zhu, V. Aji, A. Shekhter, and C. M. Varma, Phys. Rev. Lett. **100**, 057001 (2008).
[28] A. A. Kordyuk, S. V. Borisenko, M. Knupfer, and J. Fink, Phys. Rev. B **67**, 064504 (2003).
[29] W. H. Press, S. A. Teukolsky, W. T. Vetterling, and B. P. Flannery, *Numerical Recipes* (Cambridge University Press, Cambridge, 2002).
[30] A. J. Millis, H. Monien, and D. Pines, Phys. Rev. B **42**, 167 (1990).
[31] V. Aji and C. M. Varma, Phys. Rev. Lett. **99**, 067003 (2007).
[32] V. Aji and C. M. Varma, Phys. Rev. B **79**, 184501 (2009).
[33] B. Fauqué, Y. Sidis, V. Hinkov, S. Pailhès, C. T. Lin, X. Chaud, and P. Bourges, Phys. Rev. Lett. **96**, 197001 (2006).
[34] H. A. Mook, Y. Sidis, B. Fauqué, V. Balédent, and P. Bourges, Phys. Rev. B **78**, 020506(R) (2008).
[35] Y. Li, V. Baledent, N. Barisic, Y. Cho, B. Fauque, Y. Sidis, G. Yu, X. Zhao, P. Bourges, and M. Greven, Nature (London) **455**, 372 (2008).
[36] A. Kaminski *et al.*, Nature (London) **416**, 610 (2002).
[37] I. Vekhter and C. M. Varma, Phys. Rev. Lett. **90**, 237003 (2003).
[38] W. L. McMillan and J. M. Rowell, Phys. Rev. Lett. **14**, 108 (1965).